



 Cite this: *RSC Adv.*, 2021, 11, 2242

# Enhanced performance and degradation of wastewater in microbial fuel cells using titanium dioxide nanowire photocathodes

 Jingying Ma,<sup>a</sup> Donghui Chen,<sup>a</sup> \*<sup>abc</sup> Wenwen Zhang,<sup>b</sup> Zhihao An,<sup>a</sup> Ke Zeng,<sup>a</sup> Ming Yuan<sup>a</sup> and Jia Shen<sup>a</sup>

This paper explores the decolorization of dye wastewaters and electricity generation using dual-chamber microbial fuel cells (MFCs) with titanium dioxide nanowire (TiO<sub>2</sub> NW) photocathodes. TiO<sub>2</sub> NW cathodes under ultraviolet light are observed to enhance the reduction of azo dye Active Red 30 (AR 30) and electricity generation. The analysis of electrochemical impedance spectra (EIS) indicates acceleration of the electron transfer processes of photoelectrode reduction by the photocatalysis of TiO<sub>2</sub> NWs, with polarization resistance of the photocathode being 10.45 Ω under light irradiation from 294 Ω in the dark. Ultraviolet-visible light spectroscopy shows that the maximum degradation of the MFCs is 78.1%; the azo bond of AR 30 may be cleaved by photoelectrons generated by light irradiation of the illuminated TiO<sub>2</sub> NW photocathode. The electricity produced by microbial fuel cells (MFCs) is expected to enhance the reductive decolorization of the azo dye AR 30 solution.

 Received 14th October 2020  
Accepted 29th December 2020

DOI: 10.1039/d0ra08747e

[rsc.li/rsc-advances](https://rsc.li/rsc-advances)

## 1. Introduction

Synthetic azo dyes, as organic compounds with structural diversity, have been widely used in textile finishing mills. It is well known that the azo dyes have low degradability due to their high chemical, biological and photocatalytic stability.<sup>1</sup> The azo dye components remaining in the wastewater, even in low concentrations, will cause the light transmittance within the water body to decrease, which eventually leads to the destruction of the water ecosystem.<sup>2,3</sup> At present, many technologies have been used to treat azo dye wastewater, including sorbent removal,<sup>4–7</sup> coagulation/flocculation,<sup>8–11</sup> membrane separation<sup>12–17</sup> and advanced oxidation.<sup>18,19</sup> The unique advantages are respectively demonstrated in these treatment methods, however there are common problems with high energy input requirements and sludge generation. Therefore, it is imperative to develop effective treatment technology to solve the problem. As one kind of sustainable bio-electrochemical system, the area of interest in MFCs is to combine wastewater treatment and biological power generation.<sup>20</sup> Electrons are released by microorganisms to the anode in the MFC, and then transferred to the cathode by the circuit, where they combine with protons and electron acceptor (such as oxygen) to form water.<sup>21–23</sup> The microorganisms on the surface of the anode are used as

biocatalysts to reduce the overpotential as well as enhance the speed of electron transfer to the cathode, and the azo compound can be reduced in the cathode chamber.

High cathode overpotential is one of the bottlenecks in the use of MFC to reduce azo dyes, and semiconductor materials as electrode catalysts for the photoelectric degradation of azo dye wastewater are widely considered as a novel technology in enhancing the performance of MFCs.<sup>24,25</sup> In the current research, the type of powder catalyst has been widely studied. Most of the catalysts are used as electrodes in the process of constructing microbial fuel cells, therefore, powdered catalytic materials and other conductive materials must be mixed and pressed to prepare electrodes and other conductive materials can easily block light and affect the absorption of light by the catalytic material in this process. Meanwhile, poor contact may occur during the mixing process of the powder catalytic material with other materials, which affects the conduction of photoelectrodes to photogenerated electrons and holes. Here, we propose the photocatalytic material prepared by the anodic oxidation method can take advantage of the natural connection between the photocatalytic material and the titanium electrode, reducing the mixing and pressing process of the photocatalytic material and the conductive matrix and making the photocatalytic material easier to carry out on the anode. The surface of the photoelectrode stimulates the absorption of light energy, and the photo-generated holes are quickly transferred to the circuit system, thereby accelerating the overall reaction speed of the microbial fuel cell. Li *et al.*<sup>26</sup> reported the effect of the presence or absence of light on the potential generated by the MFCs coated with rutile TiO<sub>2</sub> cathode and found that the

<sup>a</sup>College of Chemical and Environmental Engineering, Shanghai Institute of Technology, Shanghai 201418, China. E-mail: chendhisit@163.com

<sup>b</sup>College of Environmental Science and Engineering, Donghua University, Shanghai 201620, China

<sup>c</sup>Institute of Foreign Languages, Shanghai Dianji University, Shanghai 201306, China



maximum potential presented in the illumination was 0.80 V while the maximum potential generated in the absence of light was 0.55 V. Long *et al.*<sup>27</sup> have systematically studied the titanium dioxide nanotube array significantly increased the power generation amount from  $3.64 \pm 0.112$  mA to  $6.246 \pm 0.135$  mA at the bioanode, which can effectively photo-catalytically degrade reactive brilliant active brilliant red X3 (ABRX3). Lu *et al.*<sup>28</sup> improved the maximum power density of the reactors under illumination was 1.6 fold, compared with dark conditions. This is the result of the enhanced cathode electron transfer by the use of semiconducting minerals, indicating that the potential of MFCs generated by light is increased. Substances of the cathodic surface, which have high redox potential, will be reduced by electrons transfer from the anode chamber. The bandwidth energy of the semiconductor materials is equal or exceeded by light energy, the electrons are excited from the valence band (VB) to the conduction band (CB) can generate the high oxidative photo-generated carriers (electron-hole pairs).<sup>29</sup> According to the mechanism, pollutants can increase the cathode redox potential, the performance of microbial fuel cells, while degrade the pollutants to achieve simultaneous degradation of the pollutants and the effect of power generation. Due to the outstanding advantages, the photoelectrodes has attracted attention of more and more researchers in the past years.<sup>30–32</sup> The Table 1 was conducted to summarize the typical research of the MFCs with photoelectrodes.

Due to its relatively stable chemical properties, biological stability, excellent electrical and optical properties, the titanium dioxide (TiO<sub>2</sub>) has been widely accepted for semiconductor catalyst material in terms of dye photocatalysis.<sup>40</sup> TiO<sub>2</sub> has been proven to be a good ORR catalyst for enhancing the performance of MFCs, used for the photocatalytic reduction of dyes wastewater in the MFCs reactor, as well as the application of photocatalysis has significantly improved the power generation performance of microbial fuel cells.<sup>41–43</sup> However, most attention has been paid to the productivity efficiency of photocatalytic microbial anodes and little information has been reported concerning cathodic reduction to produce MFCs anodes and photocathodes for pollutant degradation and electricity generation.<sup>27,34</sup>

Nanostructured photocathodes can be produced with well properties on account of the synergy effect in MFCs, including great electrical conductivity, extra apparent area and high performance.<sup>44,45</sup> In this study, the TiO<sub>2</sub> NWs photocathode of MFCs reactor were carried out the structure and photo-electrochemical properties. The systematic research was performed to analyze the output voltage, the photoelectrocatalytic activity, the degradation efficiency and mechanism of AR 30. In order to observe the electrode morphology and crystalline structure, the scanning electron microscope (SEM), the Fourier infrared spectroscopy (FT-IR) and the X-ray diffraction analysis (XRD) were applied for the characterization. In addition, the cyclic voltammetry (CV), the electrochemical impedance spectroscopy (EIS), Tafel test and the ultraviolet-visible spectrometer (UV-vis) were used to study the electricity generation and dye degradation ability of MFCs. The research further revealed the potential possibility of photocathode on improving the performance of reactor at the dye wastewater treatment combined power production of MFCs, and provide a new way for the degradation of pollutants in the reactor. We hope that the study will be useful to develop an efficient MFCs technique in azo dye-containing wastewater treatment and the development of MFC in the future.

## 2. Materials and methods

### 2.1 MFCs construction and operation

A typical dual-chamber MFC reactor was employed in this research. Each chamber was separated by cation exchange membranes (Qianqiu, Zhejiang, China) with an area of 85 cm<sup>2</sup> and constructed of two equal volumes of 100 mL rectangular plexiglass chambers (Wenote, Shanghai, China). Anode chamber was sealed with rubber stopper and cathode chamber was left with a 10 cm vent for continuous air filling continuously. Furthermore, the straight distance between anode and photocathode electrode was approximately 10 cm in microbial fuel cells and the external resistance was 22 Ω. Three different types of cathode electrodes (TiO<sub>2</sub>, TiO<sub>2</sub> NWs, plain Ti, respectively) are connected by titanium wire. The Ag/AgCl worked as a reference electrode, then a 360 nm ultraviolet light source was installed 10 cm away from the cathode (Antoine; Change

Table 1 A summary of photoelectrodes were used in MFCs

Reactor types	Photocathode design	Microbial composition	Source of inoculation	Performance	Reference
DC <sup>a</sup> /UV <sup>c</sup>	BTNA <sup>d</sup>	Proteobacteria	MFC effluent	$6.246 \pm 0.135$ mA	27
DC <sup>a</sup> /Vis <sup>b</sup>	Rutile coated graphite	MS <sup>f</sup>	Yeast extract	$16.5$ mA m <sup>-2</sup>	33
DC <sup>a</sup> /UV <sup>c</sup>	Cu <sub>2</sub> O nanowire	MS <sup>f</sup>	Freshwater sediment	$46.44$ mW m <sup>-2</sup>	34
DC <sup>a</sup> /Vis <sup>b</sup>	Pd/SiNW <sup>e</sup>	MS <sup>f</sup>	Mixed anaerobic sludge	$119$ mW m <sup>-2</sup>	35
DC <sup>a</sup> /Vis <sup>b</sup>	Pd/SiNW <sup>e</sup>	MS <sup>f</sup>	Mixed anaerobic sludge	$180119$ mW m <sup>-2</sup>	36
DC <sup>a</sup> /Vis <sup>b</sup>	Bi/TiO <sub>2</sub>	MS <sup>f</sup>	Anaerobic sludge	$224$ mW m <sup>-2</sup>	37
DC <sup>a</sup> /UV <sup>c</sup>	TiO <sub>2</sub>	MS <sup>f</sup>	Anaerobic sludge	$19.4$ mA m <sup>-2</sup>	38
DC <sup>a</sup> /UV <sup>c</sup>	Algae	Rhodospseudomonas	Wetland sediment	$202.9 \pm 18.1$ mW m <sup>-2</sup>	39

<sup>a</sup> DC, dual chambers. <sup>b</sup> Vis, visible light. <sup>c</sup> UV, ultraviolet light. <sup>d</sup> BTNA, blue titania nanotube arrays. <sup>e</sup> SiNW, p-type silicon nanowire. <sup>f</sup> MS, mixed strains.

Lighting Technology Co., Ltd., Dongguan, China). The anode chambers were inoculated with reacclimated microbial solution initially from the wetland sediment, in addition, the microbial community had been function stably for three years within the effluent from previous MFCs.<sup>34,39</sup> The anolyte was mineral salt ( $1.98 \text{ g L}^{-1}$ ,  $\text{K}_2\text{HPO}_4$  ( $6.59 \text{ g L}^{-1}$ ),  $\text{KH}_2\text{PO}_4$  ( $2.88 \text{ g L}^{-1}$ ),  $\text{C}_6\text{H}_{12}\text{O}_6$  ( $1.00 \text{ g L}^{-1}$ ) and  $\text{CH}_3\text{COONa}$  ( $1.42 \text{ g L}^{-1}$ ) and this catholyte comprised:  $\text{NaNO}_3$  ( $1.40 \text{ g L}^{-1}$ ),  $\text{NaHCO}_3$  ( $0.98 \text{ g L}^{-1}$ ),  $\text{KCl}$  ( $0.11 \text{ g L}^{-1}$ ) and Active red 30 (AR 30,  $10 \text{ mg L}^{-1}$ ). The cathode compartment in MFCs was ventilated with oxygen pumps at a gas flow rate of  $70 \text{ L h}^{-1}$  to provide sufficient oxygen for the electrochemical reaction, and distilled water was used to supplement the evaporated water every 24 hours. All MFCs reactors are operated in a  $25 \pm 2 \text{ }^\circ\text{C}$  incubator (GHP-9080, Bluepard, Shanghai, China).

## 2.2 Preparation of titanium dioxide nanowire electrode

$\text{TiO}_2$  nanowires were prepared by thermal annealing of anodized titanium plates in air. Titanium plates ( $3.0 \times 2.0 \times 0.1 \text{ cm}$ , purity 99%) were successively immersed into an aqueous solution of 15 wt% sodium hydroxide at  $60 \text{ }^\circ\text{C}$ , 30 wt% hydrochloric acid solution for pretreatment at  $100 \text{ }^\circ\text{C}$ , and then stored in deionized water or isopropyl alcohol after the ultrasonic cleaning. The pretreated titanium samples were immersed in a 5 wt%  $\text{NH}_4\text{F}$  and ethylene glycol solution and further anodized at the constant battery voltage at 30 V for 6 hours. A graphite plate was performed to use as the counter electrode and the magnetic stirrers were used in this process. After the solution turned blue, the titanium plate was washed by the deionized water, and then dried at about  $40 \text{ }^\circ\text{C}$  in the drying oven. The 100 mA cathode current was applied by an electrochemical workstation for 30 s to oxidize the electrode, which in the electrolytic solution was 0.1 M  $\text{KH}_2\text{PO}_4$ . Finally, the titanium plates were calcined at  $450 \text{ }^\circ\text{C}$  for 2 hours using the electric box resistance furnace (SX2-0.5-10A, Shaoxing, China).

## 2.3 Electrode characterizations

The apparent topography of the prepared materials was determined by employing the scanning electron microscope (SEM, JSM-5600 LV, Tokyo, Japan) at the start and the constituent elements were observed by a co-configured energy dispersive spectrometer (EDS, 20.0 kV). The crystal phases of prepared electrodes were used for the identification by the X-ray diffraction technology (XRD, Rigaku D/MAX-2550VB/PC, Tokyo, Japan). The functional groups and metal bonds contained in the sample were determined for the identification using the Fourier transform infrared spectroscopy (FT-IR, Nicolet Nexus 470, Massachusetts, America).

## 2.4 Electrochemical experiments

The test data acquisition system (BT-2016C, LANBTS, Wuhan, China) was used to record the cell output voltage level of the reactor each 30 seconds in this study. The electrochemical characteristics of the MFCs reactor with cathodic photoelectrodes were observed within third consecutive cycles in detail.<sup>46</sup> The electrochemical measurements were accurately

evaluated in order to the performance of MFCs reactor under different conditions by the electrochemical workstation methods (CHI760E, Chenhua, Shanghai, China), including the cyclic voltammetry (CV), the electrochemical impedance (EIS) and the Tafel curve. The CV in the experiment was performed to implement in a potential range of 0 to 2.0 V (vs. Ag/AgCl) with the sweeping rate of  $10\text{--}80 \text{ mV s}^{-1}$  under different test systems. The titanium dioxide nanowires, graphite and Ag/AgCl (sat. KCl) were separately used as the work electrode, counter electrode and reference electrode in standard three-electrode and the titanium dioxide nanowires, graphite were used as the work electrode, counter electrode in two-electrode system. The EIS was performed (10 Hz to 500 kHz) to calculate the resistance of electrodes and then the fitting calculation data were received with Z-SimpWin software by using a suitable model. The Tafel plots was investigated within the overpotential range of 0.5 to  $-0.5 \text{ mV}$  with a sweeping rate at  $1 \text{ mV s}^{-1}$  to evaluate the corrosion resistance of cathodic materials. In addition, we used the electrochemical measurements for the anode compartment in the microbial fuel cells under anaerobic/anoxic conditions, which based on the open circuit was carried out to maintain a continuous output voltage before the electrochemical test.

## 2.5 Photoelectrocatalytic degradation experiments

After the MFCs reactor were constructed, the carbon felt cathode was replaced with a titanium dioxide nanowires or titanium electrodes. The azo dye AR 30 was used as a model organic pollutant in order to determine the photoelectrochemical degradation of the MFCs. The 100 mL of  $10 \text{ mg L}^{-1}$  AR 30 solutions were carried out to enter the cathodic chamber, then irradiated with an ultraviolet light source at a distance of 10 cm. The  $22 \text{ } \Omega$  external resistor was used to the connection of the anode and cathode electrode, and then a data acquisition system was used to monitor the voltage of MFCs. During the experiments, the samples of the cathode chamber were extracted every 1 hour and analyzed the concentration of azo dye AR 30 by the ultraviolet-visible light spectrophotometer (UV-vis, TU-3900). The absorption wavelength of the dye solution was determined to be 540 nm.

# 3. Results and discussion

## 3.1 Characterization of photocathode

The scanning electron microscope (SEM) analysis can be performed to characterize the microscopic surface and structure of the sample. The microtopography of  $\text{TiO}_2$  nanowires electrodes was investigated using SEM-EDS and the images are shown in Fig. 1(a and b). The hollow  $\text{TiO}_2$  NWs grows on the substrate thickly, and it is well known that the nanowires can be used for the transfer process of electrons as the effective structure which has been shown to be an efficient structure for electron transfer processes.<sup>25</sup> Fig. 1(a and b) is the image of a  $\text{TiO}_2$  NWs photoelectrode, it is easy to find that the nanowire structure is relatively complete, and the shape is regular, and the size is relatively uniform. The average diameter is  $0.56 \text{ } \mu\text{m}$ , and they overlap each other to form a thin film. The titanium dioxide

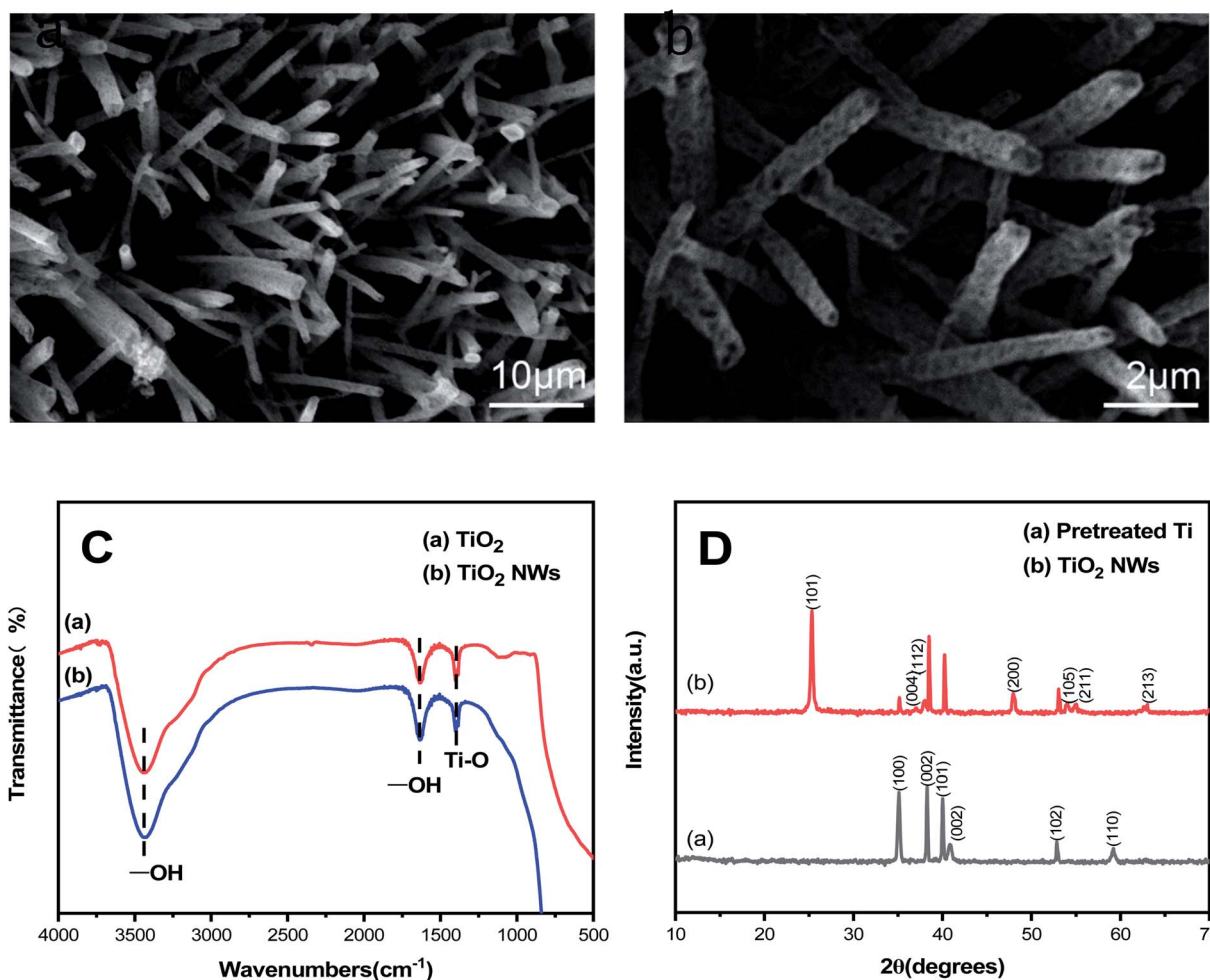


Fig. 1 (a and b) SEM image of the TiO<sub>2</sub> NWs electrode. (c) FTIR spectra of commercial titanium dioxide and TiO<sub>2</sub> NWs electrode. (d) XRD pattern after pretreatment.

nanowires may progressively grow on the appearance of titanium plate by electrochemical etching reaction. The chemical composition and stoichiometry of photoelectrodes were examined by EDS, the elemental composition of titanium dioxide nanowire photoelectrode, which is in accordance with the operating conditions.

FT-IR spectroscopy was employed to prove the properties of the prepared materials. Prepared photoelectrodes show practically the similar spectrum as commercial titanium dioxide, which shows that titanium dioxide materials have high purity in Fig. 1(c). Specifically, the significant peaks at  $3444.99\text{ cm}^{-1}$  and  $1603.44\text{ cm}^{-1}$  were accorded with the -OH stretching vibration and the -OH bending vibration absorption. Thus, the significant peak at  $697.19\text{ cm}^{-1}$  was accorded with the vibration absorption of Ti-O. Due to the position of the characteristic peak of the prepared titanium dioxide nanowire shifted to high frequency, the absorption peak of TiO<sub>2</sub> became wider and the weak peak of the electrode was clearly presented, which certified that the electrode conductivity can be increased by preparing nanowires.

As shown in Fig. 1(d), XRD further confirmed the crystal phase of the obtained sample. The crystalline structure of titanium dioxide nanowire was analyzed, comparing with commercial titanium dioxide. Three distinct reflections attributed to Ti observed at  $35.113^\circ$ ,  $38.254^\circ$ , and  $40.005^\circ$ , which can be described to the Ti tetragonal (JCPDS no. 44-1294). The peak at  $41.098^\circ$  corresponded to (002) is titanium hydride (JCPDS no. 25-0983). Titanium hydride was formed on the surface of the pretreated titanium plate, which can increase the real area of the substrate and the working life of the electrode compared with a smooth electrode. Additionally, the diffraction peak of photoelectrode at  $25.332^\circ$ ,  $38.080^\circ$ ,  $38.474^\circ$ ,  $47.970^\circ$ ,  $54.060^\circ$ ,  $55.027^\circ$ ,  $62.619^\circ$  can be indexed with the TiO<sub>2</sub> tetragonal (JCPDS no. 21-1272). The pattern revealed the structure of electrodes with peaks at  $2\theta = 25.332^\circ$ ,  $38.474^\circ$ , and  $47.970^\circ$  corresponded to (101), (112) and (200) indexed with anatase-phase titanium dioxide. The remaining peaks at  $38.080^\circ$ ,  $54.060^\circ$ ,  $55.027^\circ$ , and  $62.619^\circ$  corresponded to (004), (105), (211), and (213) are rutile titanium dioxide. The crystallite size of the TiO<sub>2</sub> NWs electrode was calculated exactly by means of the Debye-Scherrer's eqn (1),



$$D = \frac{0.9\lambda}{\beta \cos \theta} \quad (1)$$

In this formula,  $D$ ,  $\lambda$ ,  $\beta$  and  $\theta$  are the crystalline size in the direction perpendicular to the lattice planes, the wavelength of the  $\text{CuK}\alpha$  line, the full-width at half maxima intensity of the peak and the Bragg angle, separately. In addition, the default value of  $\lambda$  was given as 0.154 nm in the case of  $\text{CuK}\alpha$ . The calculation results were shown that the crystallite size of anatase and rutile  $\text{TiO}_2$  were respectively estimated to be 570.89 nm and 505.05 nm according to this equation and then the reduction of crystallite size and the increase of specific surface area may effectively promote the progress of the PEC reaction as well as the photocatalysis of the rutile titanium dioxide enhanced cathodic electron transfer.<sup>28</sup>

### 3.2 Electrochemical characterization of photoelectrode

It is seen clearly from Fig. 2 that the titanium dioxide nanowires have capacitive performance in a three-electrode configuration and may be easily applied to the symmetric capacitor. According to the cyclic voltammetry curves in two-electrode model, it can be inferred that the nearly quasi-rectangular curves have the wide working potential window in MFCs.<sup>47</sup> Fig. 2(a–c) shows that the area of the voltammogram follows the order of open circuit > cathode > anode, which indicates that the titanium dioxide nanowire electrode cathode has great potential in catalyzing ORR.

The electrochemical impedance spectroscopy was carried out the effect of illumination on the charge transfer performance of different electrodes, the analysis of electrodes was performed under dark and ultraviolet light irradiation. The Nyquist plots of electrodes was fitted by different equivalent circuits under dark/light conditions. The impedance of the sample was represented by the radius of curvature of the curve, the larger the radius of the curve, the greater the impedance of the sample, and the smaller the number of electrons moving in the electrochemical circuit. As shown in Fig. 2, it can be inferred that the MFCs using the titanium dioxide nanowires have higher rate of promoting electron transfer compared to titanium plate electrodes. The calculated results of electrodes from Nyquist plots were shown in Table 2 by fitting the equivalent circuit model in Fig. 3. The EIS results of open/closed MFCs under a dark condition were analyzed using the  $R_1(\text{CPE}_1R_2)W$  model, in which  $\text{CPE}_1$  representing the electrode capacitance and  $R_2$  representing the polarization resistance were composed the parallel combination, and  $R_1$  corresponding to the ohmic resistance was connected in series with them. In the open circuit condition of MFCs, the  $R_2$  value of titanium electrode was 2 fold larger than the  $\text{TiO}_2$  NWs cathode. The fitting model  $R_1(\text{CPE}_1R_2)(\text{CPE}_2R_3)W$  was performed to analyze the results under lighting conditions, in which  $R_3$  and  $\text{CPE}_2$  represent oxide layer resistance and oxide layer capacitor, respectively. Compared with the titanium electrodes of MFCs under dark conditions, the  $R_2$  value of the  $\text{TiO}_2$  NWs cathodic electrode was estimated to be 292.4  $\Omega$ . It can be inferred that the polarization resistance of the  $\text{TiO}_2$  NWs cathodic electrode under above two fitting modes was significantly lower than the titanium cathode

in the same bio-electrochemical system. The  $R_3$  value of MFCs with  $\text{TiO}_2$  NWs cathodic electrode under illumination was significantly reduced to 10.45  $\Omega$ , which prove that the conductivity of the  $\text{TiO}_2$  NWs cathodic electrode increases sharply and the PEC activity of the titanium dioxide was considered to be the possible reason. The data fitting results of the Z-SimpWin software were performed to indicate the polarization resistance of  $\text{TiO}_2$  NWs electrode in closed circuit was significantly reduced and the conductivity cathodic electrode increases sharply, which proved that the largest electrochemical active points was considered to be the possible reason.<sup>48</sup> It can be inferred that the main reason for the exaltation of the power production with  $\text{TiO}_2$  NWs may be the high electron transference in the light irradiation.<sup>49</sup>

Tafel polarization curves were used to analyze the influence of current density for the corrosion resistance of MFCs cathode materials. It is clear from Table 3, the electrochemical corrosion parameters were calculated by fitting the polarization curve Tafel region, including the corrosion potential ( $E_{\text{corr}}$ ), the self-corrosion current density ( $I_{\text{corr}}$ ) and the polarization resistance ( $R_p$ ). The  $E_{\text{corr}}$  of metals was inversely proportional to the corrosion tendency, and the magnitude of the corrosion rate was related to the metal polarization phenomenon while the  $I_{\text{corr}}$  of the electrode was proportional to the corrosion rate of the system and inversely proportional to the corrosion resistance. Observation of the Tafel curve in Fig. 2(e) shows that titanium dioxide nanowire has the lowest corrosion current density, indicating good corrosion resistance and provides a good basis for further photodegradation experiments.

The continuing steady process of electrodes was correspondingly vital symbol to estimate the activity of MFCs in the research. Hence, the voltage output of MFCs in closed circuit under the intermittent method was accurately monitored by a data acquisition system in order to observe the stable and durable performance of the electrodes. Fig. 2(f) shows that the voltage can be maintained at the highest pressure of 8–12 days for each cycle, and the electrodes can be maintained of continuous operation at such current densities.<sup>50</sup> Furthermore, the microbial fuel cells with  $\text{TiO}_2$  NWs cathode exposed the maximum voltage output level of  $221 \pm 0.02$  mV, which was 23.76 and 1.43 times of that of Ti ( $9.3 \pm 0.02$  mV) and commercial  $\text{TiO}_2$  ( $154.37 \pm 0.02$  mV), separately. The better coulombic efficiency was generally expressed as a higher voltage output levels and the MFCs with  $\text{TiO}_2$  NWs photoelectrode was proven to get a large amount of energy using data acquisition system. The MFCs reactors in this study were determined for long-term operation (about 50 d) in a constant temperature incubator, which the voltage output level was controlled stability within each operating cycle. Furthermore, the test results indicated that  $\text{TiO}_2$  NWs photoelectrode was relatively proven the greatest stability and durability of photoelectrodes in microbial fuel cells.

### 3.3 The optical absorption characteristics of electrodes

As is shown in Fig. 4, the diffuse reflectance spectra of pre-treated titanium plates and  $\text{TiO}_2$  NWs. The optical absorption

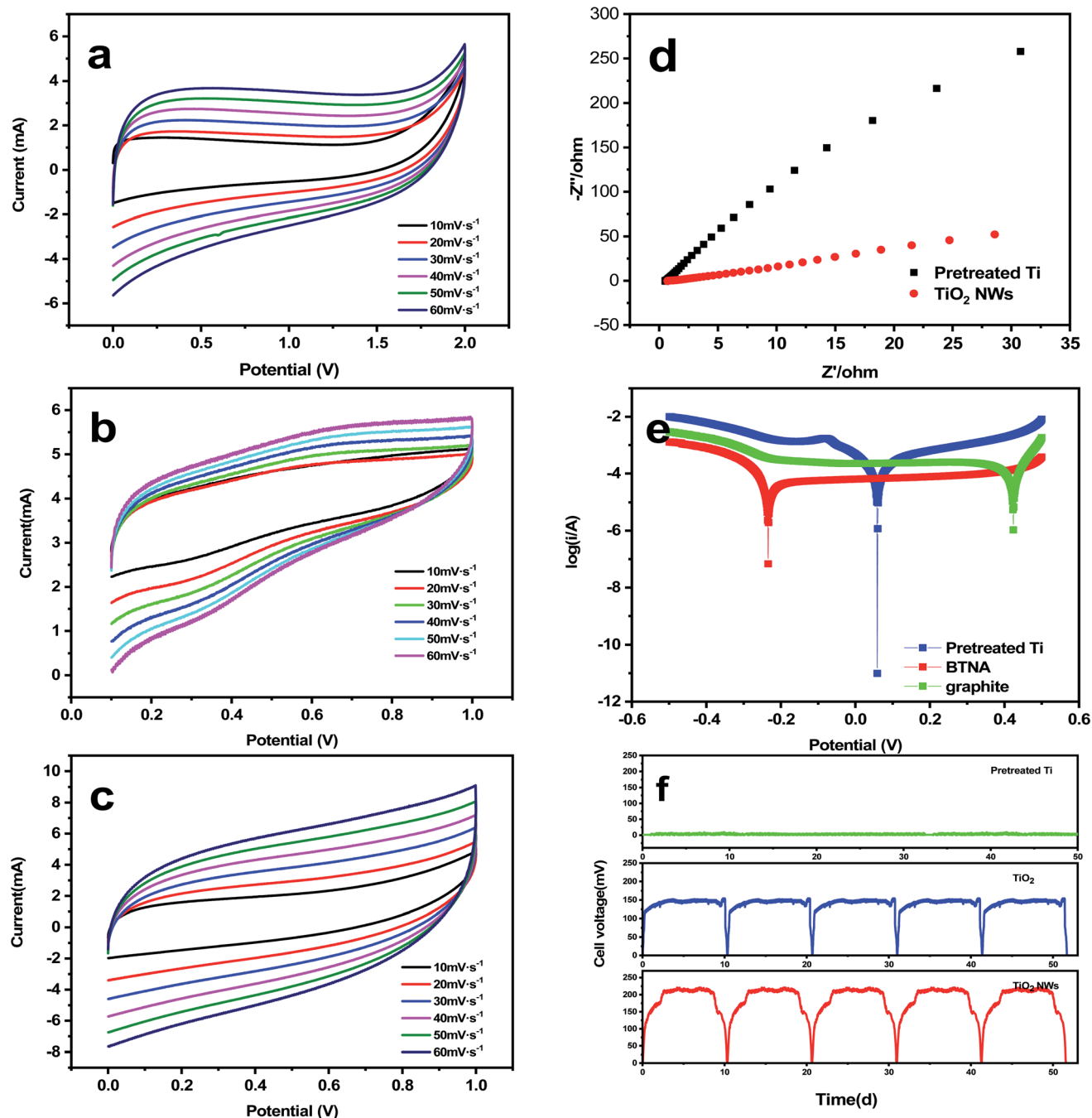


Fig. 2 Electrochemical tests in electrolyte. (a) CV curves of TiO<sub>2</sub> NWs electrode electrolyte in three-electrode mode. (b) CV curves of TiO<sub>2</sub> NWs anode in two-electrode mode. (c) CV curves of TiO<sub>2</sub> NWs cathode in two-electrode mode. (d) Nyquist plots of different electrodes and equivalent circuits used to fit the EIS data. (e) Tafel polarization curves of different electrode. (f) The cells voltage over time under external resistance.

Table 2 The fitting results of different cathodes electrodes from Nyquist plots

Cathodes	$R_2/\Omega \text{ cm}^{-2}$	$\text{CPE}/\Omega \text{ cm}^{-2} \text{ S}^n$	(A) Dark conditions		(B) Under illumination	
			$R_2/\Omega \text{ cm}^{-2}$	$\text{CPE}/\Omega \text{ cm}^{-2} \text{ S}^n$	$R_3/\Omega \text{ cm}^{-2}$	$\text{CPE}/\Omega \text{ cm}^{-2} \text{ S}^n$
Pretreated Ti	9901	$9.132 \times 10^{-5}$	3650	$9.84 \times 10^{-4}$	18.56	$3.90 \times 10^{-3}$
TiO <sub>2</sub> NWs	4849	$6.132 \times 10^{-5}$	292.4	$3.26 \times 10^{-2}$	10.45	$1.56 \times 10^{-1}$

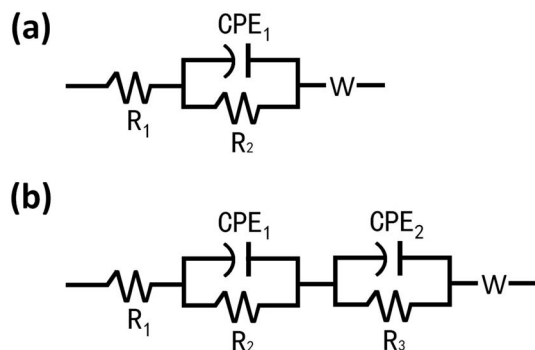


Fig. 3 Equivalent circuit models were used in the analysis of electrodes in MFCs (a) under the dark conditions (b) under illumination.

Table 3 Corrosion parameters of different electrodes

	$E_{\text{corr}}$ (vs. SCE)/V	$I_{\text{corr}}$ /( $\mu\text{A cm}^{-2}$ )	$R_p$ /( $\text{k}\Omega \text{ cm}^2$ )
Graphite	0.426	17.6	1481.5
Pretreated Ti	0.061	8.4	2333.7
TiO <sub>2</sub> NWs	-0.231	2.4	193.1

characteristics of the pretreated titanium plates and TiO<sub>2</sub> NWs photoelectrodes were investigated by using UV-vis DRS as well as the test result was presented in Fig. 4(a). TiO<sub>2</sub> NWs can absorb light more strongly after anodizing. The absorption of ultraviolet light (<350 nm) and ultraviolet light (>400 nm) in TiO<sub>2</sub> NWs is obviously enhanced compared with pretreated titanium plates.

The applicable conditions were affected by the size of the material band gap. Therefore, the UV-vis DRS data was used to calculate the band gap energy value of electrode materials based on formula (2) and the calculated results were shown in Fig. 4(b and c):

$$\alpha h\nu = \beta(h\nu - E_g)^{(m/2)} \quad (2)$$

where  $\alpha$  is the absorption coefficient,  $\beta$  is a proportional constant related to the band tailing parameter,  $h\nu$  is the incident photon energy related to Planck constant and  $E_g$  is the indirect optical energy gap. The  $m$  is related to the semiconductor materials as well the type of transition,  $m = 1$  and  $m = 4$  corresponded to the direct band gap semiconductor materials and the indirect band gap materials, respectively. Titanium dioxide is generally regarded as an indirect bandgap semiconductor and the energy ( $h\nu$ ) and  $(\alpha h\nu)^2$  can be used as coordinate axes to draw the forbidden bands diagram of titanium dioxide and titanium. As can be seen from Fig. 4(b and c), the band gap values of the pretreated titanium plates and the prepared titanium dioxide nanotubes are approximately 2.84 eV and 3.22 eV, respectively, which are correspond to the results of previous journal studies.<sup>51</sup>

### 3.4 The degradation performance of photoelectrodes

The degradation performance of TiO<sub>2</sub> NWs photoelectrode in MFCs for azo dyes was evaluated by UV-vis spectrophotometer. The results of the spectral scanning results over time were shown in Fig. 5(a) by using photoelectrode to degrade the dye AR 30 solution under illumination. It is can be obviously inferred that the strength of the feature peak corresponding to the azo structure of the dye AR 30 gradually declines over time increases. The feature peak of the azo structure was performed to virtually disappear after 6 hours of degradation, which proves that the photoelectrode possess the well photocatalytic degradation performance of the azo dye AR 30 solution in microbial fuel cells.<sup>52</sup>

Fig. 5(b) illustrates the degradation degree of azo dye AR 30 by TiO<sub>2</sub> NWs photocathode under different conditions of MFCs.

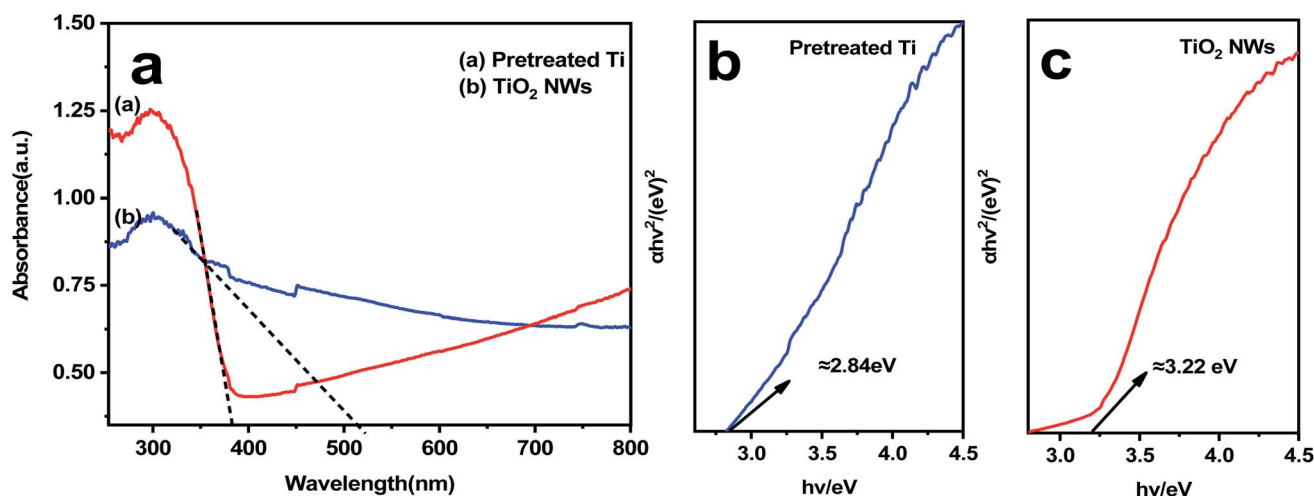


Fig. 4 (a) UV-visible light absorption DRS patterns, (b) calculated energy bandgap of pretreated titanium plates, (c) calculated energy bandgap of TiO<sub>2</sub> NWs.

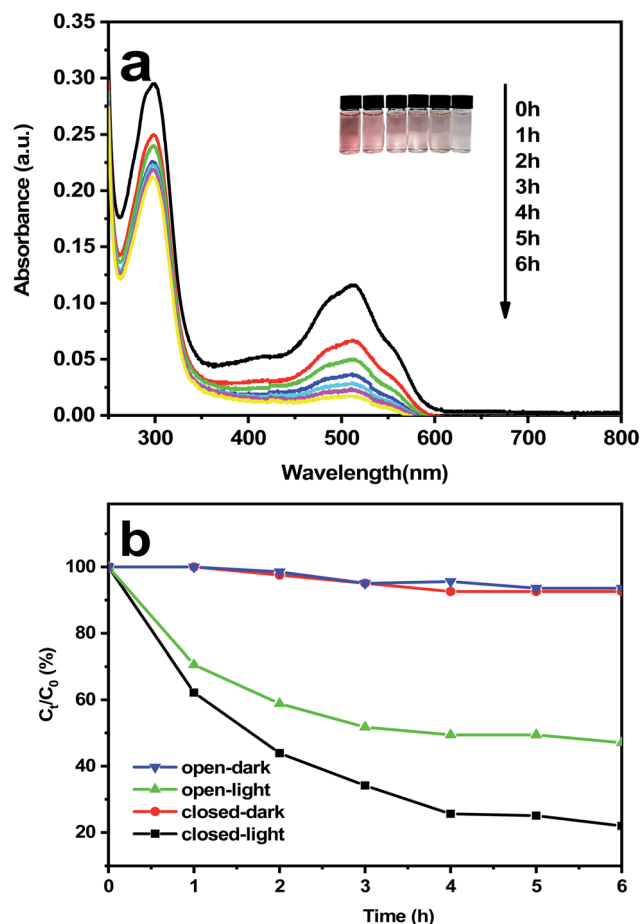


Fig. 5 (a) Photo images of AR 30 in the photodegradation; (b) degradation efficiency curve during open/closed circuit/light-dark conversion.

From the curve, we can see that the photocatalytic degradation effect is different under various operating conditions. It can be shown from the degradation curve that the maximum degradation rate of MFCs were 52.95% and 78.1% under open circuit

and turnover conditions, respectively. Meanwhile, the maximum degradation of the MFCs under light irradiation was 1.47 times stronger than in the darkness. The results show that the photocathode in MFCs has the highest degradation rate of dyes after 6 hours of ultraviolet irradiation, and the best decolorization performance was obtained. The main reason may be the enhancement of the decolorization of the dye by the light-induced electrons. It can be inferred that the  $\text{TiO}_2$  NWs photoelectrode under the excitation of ultraviolet light generated the electron-hole pairs, and then the free charge carriers were separated. In addition, the results of monitoring the degradation of azo dyes in the cathode compartment showed the  $\text{TiO}_2$  NWs electrodes under ultraviolet photoexcitation had a catalytic process to degrade the azo dye. Therefore, a relatively high degradation rate of MFCs can be achieved by this photocatalytic process, and the photogenerated holes ( $h_{\text{VB}}^+$ ) of the electrode in the cathode chamber enhanced the reaction rate by the electrons ( $e_{\text{CB}}^-$ ), the output voltage of MFCs were increased, as well as the internal resistance was decreased.

To more comprehensively examine the performance of  $\text{TiO}_2$  NWs, the comparison of polarization and power density (PD) curves in MFCs with photoelectrodes under light and dark was shown in Fig. 6(a). The results show that the maximum PD curves of the MFCs were 23.41 and 45.63  $\text{mW m}^{-2}$ , under light and dark condition, respectively. The maximum power density under light conditions was approximately twice that under dark conditions. It can be inferred that the catalytic efficiency of photoelectrodes substantially enhance in the light compared to the dark, and the further shows that light can be beneficial to increase the power production of the reactor. The instantaneous photocurrent response curve of the prepared photoelectrodes under ultraviolet irradiation was shown in Fig. 6(b). The curve showed that the photocurrent response with the  $\text{TiO}_2$  NWs sample was particularly obvious, and the test time interval between the light-dark transitions was 20 s. Usually, the separation capability of electrons and holes pairs is proportional to the photocurrent density, which has a significant effect on the improvement of photocatalytic activity. The stronger

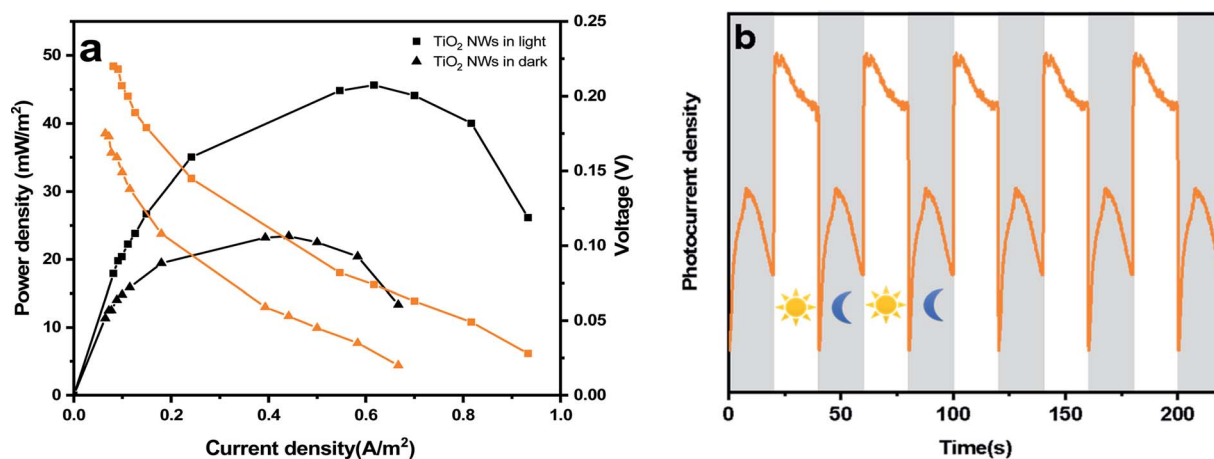


Fig. 6 (a) The power curve of MFCs with  $\text{TiO}_2$  photocathode under light and dark. (b) Transient photocurrent responses of MFCs with  $\text{TiO}_2$  NWs photocathode.



photocurrent response intensity of photoelectrodes was presented from the curve and the large local micro-regions may be the main reason, which has a positive effect on the separation/transmission of electrons and holes as well as further increases the production capacity of microbial fuel cells.

Due to the cleavage of the azo bond, the degradation product of AR 30 in MFCs was a reductive product, indicating that the photo-generated holes generated by the photoelectrode are directly consumed by the electrons from the anode. The generated photo-generated electrons and the excess electrons transferred from the anode participated in the process of organic reduction, realizing the bond breaking and decolorization of AR 30. Under aerobic conditions, O<sub>2</sub> and AR 30 competed to become the electron acceptor. However, O<sub>2</sub> had a higher redox potential and preferentially reacted with the electrons transferred from the anode, resulting in a higher cathode reduction potential and electricity generation performance. The strong oxidizing free radicals generated in the process affected the oxidative degradation of organic matter. The remaining electrons reacted with AR 30 to achieve reduction and decolorization.

## 4. Conclusion

In this research, the dye degradation and electricity generation were studied in MFCs by employing the prepared TiO<sub>2</sub> nanowires photocathode. The charge transfer performance of prepared materials was evaluated through electrochemical measurement. The results showed that the photoelectrode exhibited high output voltage and low internal resistance in the reactor of MFCs under illumination. The anticorrosion of TiO<sub>2</sub> NWs photoelectrode as the cathode contributed to the long-time operation (about 50 d) of MFCs in constant temperature incubator (25 ± 2 °C). The photocathode significantly promoted the separation of azo bonds and degradation of AR 30. The possible mechanism of the whole photocathodic MFCs could be explained as follows: under light irradiation, the photo-generated electrons of the cathode were released and reacted with the terminal electron acceptor, thus leaving the photo-generated holes as electron acceptors. These holes, combined with the electrons transferred from the anode, led to the accelerated reaction of cathode, the increased output voltage and the decreased internal resistance. Therefore, the photoelectrode in this study can be used as a safer and cleaner microbial fuel cell (MFCs) to treat dye wastewater and generate electricity at the same time in the future.

## Conflicts of interest

There are no conflicts to declare.

## Acknowledgements

The authors would like to express appreciation for the Innovation Project of College Students Science and Technology provided by Shanghai Institute of Technology (no. DCX2019198) and the University Funded Project of Shanghai (no. 50578020).

Manhong Huang (Donghua University) are gratefully acknowledged to conduct the research work for the experimental guidance support.

## References

- 1 J. M. S. Oliveira, E. S. M. R. de Lima, C. G. Issa, J. J. Corbi, M. Damianovic and E. Foresti, Intermittent aeration strategy for azo dye biodegradation: a suitable alternative to conventional biological treatments?, *J. Hazard. Mater.*, 2020, **385**, 121558.
- 2 C. R. Holkar, A. J. Jadhav, D. V. Pinjari, N. M. Mahamuni and A. B. Pandit, A critical review on textile wastewater treatments: possible approaches, *J. Environ. Manage.*, 2016, **182**, 351–366.
- 3 F. C. Moreira, R. A. R. Boaventura, E. Brillas and V. J. P. Vilar, Electrochemical advanced oxidation processes: a review on their application to synthetic and real wastewaters, *Appl. Catal., B*, 2017, **202**, 217–261.
- 4 S. Wong, H. H. Tumari, N. Ngadi, N. B. Mohamed, O. Hassan, R. Mat and N. A. Saidina Amin, Adsorption of anionic dyes on spent tea leaves modified with polyethyleneimine (PEI-STL), *J. Cleaner Prod.*, 2019, **206**, 394–406.
- 5 N. Hou, R. Wang, R. Geng, F. Wang, T. Jiao, L. Zhang, J. Zhou, Z. Bai and Q. Peng, Facile preparation of self-assembled hydrogels constructed from poly-cyclodextrin and poly-adamantane as highly selective adsorbents for wastewater treatment, *Soft Matter*, 2019, **15**, 6097–6106.
- 6 D. Jiang, M. Chen, H. Wang, G. Zeng, D. Huang, M. Cheng, Y. Liu, W. Xue and Z. Wang, The application of different typological and structural MOFs-based materials for the dyes adsorption, *Coord. Chem. Rev.*, 2019, **380**, 471–483.
- 7 Y. Zheng, B. Cheng, J. Fan, J. Yu and W. Ho, Review on nickel-based adsorption materials for Congo red, *J. Hazard. Mater.*, 2020, **403**, 123559.
- 8 K. Guo, Y. Gao, B. Gao, Q. Feng, X. Shen, C. Liu, Q. Yue and X. Xu, Structure-activity relationships of the papermill sludge-based flocculants in different dye wastewater treatment, *J. Cleaner Prod.*, 2020, 266.
- 9 D. Luan, L. Wu, T. Wei, L. Liu, Y. Lv, F. Yu, L. Chen and Y. Shi, N, S Dual-Doped carbon derived from dye sludge by using polymeric flocculant as soft template, *Nanomaterials*, 2019, **9**, 991.
- 10 V. Bisht and B. Lal, Exploration of performance kinetics and mechanism of action of a potential novel bioflocculant BF-VB2 on clay and dye wastewater flocculation, *Front. Microbiol.*, 2019, **10**, 1288.
- 11 J. Dotto, M. R. Fagundes-Klen, M. T. Veit, S. M. Palácio and R. Bergamasco, Performance of different coagulants in the coagulation/flocculation process of textile wastewater, *J. Cleaner Prod.*, 2019, **208**, 656–665.
- 12 J. Lin, W. Ye, M.-C. Baltaru, Y. P. Tang, N. J. Bernstein, P. Gao, S. Balta, M. Vlad, A. Volodin, A. Sotto, P. Luis, A. L. Zydny and B. Van der Bruggen, Tight ultrafiltration membranes for enhanced separation of dyes and

- Na<sub>2</sub>SO<sub>4</sub> during textile wastewater treatment, *J. Membr. Sci.*, 2016, **514**, 217–228.
- 13 M. A. Laqbaqbi, M. C. García-Payo, M. Khayet, J. El Kharraz and M. Chaouch, Application of direct contact membrane distillation for textile wastewater treatment and fouling study, *Sep. Purif. Technol.*, 2019, **209**, 815–825.
- 14 D. Guo, Y. Xiao, T. Li, Q. Zhou, L. Shen, R. Li, Y. Xu and H. Lin, Fabrication of high-performance composite nanofiltration membranes for dye wastewater treatment: mussel-inspired layer-by-layer self-assembly, *J. Colloid Interface Sci.*, 2020, **560**, 273–283.
- 15 X. Zhang, H. Li, J. Wang, D. Peng, J. Liu and Y. Zhang, *In situ* grown covalent organic framework nanosheets on graphene for membrane-based dye/salt separation, *J. Membr. Sci.*, 2019, **581**, 321–330.
- 16 J. Li, S. Yuan, J. Zhu and B. Van der Bruggen, High-flux, antibacterial composite membranes *via* polydopamine-assisted PEI-TiO<sub>2</sub>/Ag modification for dye removal, *Chem. Eng. J.*, 2019, **373**, 275–284.
- 17 D. Ji, C. Xiao, S. An, J. Zhao, J. Hao and K. Chen, Preparation of high-flux PSF/GO loose nanofiltration hollow fiber membranes with dense-loose structure for treating textile wastewater, *Chem. Eng. J.*, 2019, **363**, 33–42.
- 18 W. Yu, Y. Liu, Y. Xu, R. Li, J. Chen, B.-Q. Liao, L. Shen and H. Lin, A conductive PVDF-Ni membrane with superior rejection, permeance and antifouling ability *via* electric assisted *in situ* aeration for dye separation, *J. Membr. Sci.*, 2019, **581**, 401–412.
- 19 T. Tavangar, K. Jalali, M. A. Alaei Shahmirzadi and M. Karimi, Toward real textile wastewater treatment: membrane fouling control and effective fractionation of dyes/inorganic salts using a hybrid electrocoagulation – Nanofiltration process, *Sep. Purif. Technol.*, 2019, **216**, 115–125.
- 20 T. Cai, L. Meng, G. Chen, Y. Xi, N. Jiang, J. Song, S. Zheng, Y. Liu, G. Zhen and M. Huang, Application of advanced anodes in microbial fuel cells for power generation: a review, *Chemosphere*, 2020, **248**, 125985.
- 21 B. E. Logan, *Microbial Fuel Cells*, John Wiley & Sons, Hoboken, New Jersey, 2008.
- 22 H. Wang, B. Fu, J. Xi, H. Y. Hu, P. Liang, X. Huang and X. Zhang, Remediation of simulated malodorous surface water by columnar air-cathode microbial fuel cells, *Sci. Total Environ.*, 2019, **687**, 287–296.
- 23 B. Fu, T. Xu, X. Guo, P. Liang, X. Huang and X. Zhang, Optimization and simulation of a carbon-based flow-through composite anode configuration to enhance power generation and improve effluent quality simultaneously for microbial fuel cells, *J. Cleaner Prod.*, 2019, **229**, 542–551.
- 24 N. V. Ryzhkov, V. Y. Yurova, S. A. Ulasevich and E. V. Skorb, Photoelectrochemical photocurrent switching effect on a pristine anodized Ti/TiO<sub>2</sub> system as a platform for chemical logic devices, *RSC Adv.*, 2020, **10**, 12355–12359.
- 25 S. Choi, J. Hwang, T. H. Lee, H.-H. Kim, S.-P. Hong, C. Kim, M.-J. Choi, H. K. Park, S. S. M. Bhat, J. M. Suh, J. Lee, K. S. Choi, S.-H. Hong, J. C. Shin and H. W. Jang, Photoelectrochemical hydrogen production at neutral pH phosphate buffer solution using TiO<sub>2</sub> passivated InAs Nanowire/p-Si heterostructure photocathode, *Chem. Eng. J.*, 2020, 392.
- 26 Y. Li, A. Lu, H. Ding, S. Jin, Y. Yan, C. Wang, C. Zen and X. Wang, Cr(vi) reduction at rutile-catalyzed cathode in microbial fuel cells, *Electrochem. Commun.*, 2009, **11**, 1496–1499.
- 27 X. Long, H. Wang, C. Wang, X. Cao and X. Li, Enhancement of azo dye degradation and power generation in a photoelectrocatalytic microbial fuel cell by simple cathodic reduction on titania nanotube arrays electrode, *J. Power Sources*, 2019, **415**, 145–153.
- 28 A. Lu, Y. Li, S. Jin, H. Ding, C. Zeng, X. Wang and C. Wang, Microbial fuel cell equipped with a photocatalytic rutile-coated cathode, *Energy Fuels*, 2010, **24**, 1184–1190.
- 29 J. Xu, C. C. Boyd, Z. J. Yu, A. F. Palmstrom, D. J. Witter, B. W. Larson, R. M. France, J. Werner, S. P. Harvey, E. J. Wolf, W. Weigand, S. Manzoor, M. F. A. M. v. Hest, J. J. Berry, J. M. Luther, Z. C. Holman and M. D. McGehee, Triple-halide wide-band gap perovskites with suppressed phase segregation for efficient tandems, *Science*, 2020, **367**, 1097–1104.
- 30 D. Chen, Z. Liu, Z. Guo, W. Yan and M. Ruan, Decorating Cu<sub>2</sub>O photocathode with noble-metal-free Al and NiS cocatalysts for efficient photoelectrochemical water splitting by light harvesting management and charge separation design, *Chem. Eng. J.*, 2020, 381.
- 31 H. She, P. Yue, X. Ma, J. Huang, L. Wang and Q. Wang, Fabrication of BiVO<sub>4</sub> photoanode cocatalyzed with NiCo-layered double hydroxide for enhanced photoactivity of water oxidation, *Appl. Catal., B*, 2020, 263.
- 32 Y. Liu, M. Lai, L. Long, Y. Zhang, L. Luo, F. Shen, X. Zhang, S. Zhang, S. Deng and X. Chen, Photonic TiO<sub>2</sub> photoelectrodes for environmental protections: can color be used as a quick selection indicator for photoelectrocatalytic performance?, *J. Hazard. Mater.*, 2020, 398.
- 33 H. Ding, Y. Li, A. Lu, S. Jin, C. Quan, C. Wang, X. Wang, C. Zeng and Y. Yan, Photocatalytically improved azo dye reduction in a microbial fuel cell with rutile-cathode, *Bioresour. Technol.*, 2010, **101**, 3500–3505.
- 34 Z. Sun, R. Cao, M. Huang, D. Chen, W. Zheng and L. Lin, Effect of light irradiation on the photoelectricity performance of microbial fuel cell with a copper oxide nanowire photocathode, *J. Photochem. Photobiol., A*, 2015, **300**, 38–43.
- 35 H.-X. Han, C. Shi, L. Yuan and G.-P. Sheng, Enhancement of methyl orange degradation and power generation in a photoelectrocatalytic microbial fuel cell, *Appl. Energy*, 2017, **204**, 382–389.
- 36 H. X. Han, C. Shi, N. Zhang, L. Yuan and G. P. Sheng, Visible-light-enhanced Cr(vi) reduction at Pd-decorated silicon nanowire photocathode in photoelectrocatalytic microbial fuel cell, *Sci. Total Environ.*, 2018, **639**, 1512–1519.
- 37 G. D. Bhowmick, M. T. Noori, I. Das, B. Neethu, M. M. Ghangrekar and A. Mitra, Bismuth doped TiO<sub>2</sub> as an excellent photocathode catalyst to enhance the

- performance of microbial fuel cell, *Int. J. Hydrogen Energy*, 2018, **43**, 7501–7510.
- 38 Z. Q. Lin, S. J. Yuan, W. W. Li, J. J. Chen, G. P. Sheng and H. Q. Yu, Denitrification in an integrated bioelectro-photocatalytic system, *Water Res.*, 2017, **109**, 88–93.
- 39 W. Zheng, T. Cai, M. Huang and D. Chen, Comparison of electrochemical performances and microbial community structures of two photosynthetic microbial fuel cells, *J. Biosci. Bioeng.*, 2017, **124**, 551–558.
- 40 P. S. Basavarajappa, S. B. Patil, N. Ganganagappa, K. R. Reddy, A. V. Raghu and C. V. Reddy, Recent progress in metal-doped TiO<sub>2</sub>, non-metal doped/codoped TiO<sub>2</sub> and TiO<sub>2</sub> nanostructured hybrids for enhanced photocatalysis, *Int. J. Hydrogen Energy*, 2020, **45**, 7764–7778.
- 41 S. A. A. Yahia, L. Hamadou, M. J. Salar-García, A. Kadri, V. M. Ortiz-Martínez, F. J. Hernández-Fernández, A. P. de los Ríos and N. Benbrahim, TiO<sub>2</sub> nanotubes as alternative cathode in microbial fuel cells: effect of annealing treatment on its performance, *Appl. Surf. Sci.*, 2016, **387**, 1037–1045.
- 42 C. V. Reddy, K. R. Reddy, N. P. Shetti, J. Shim, T. M. Aminabhavi and D. D. Dionysiou, Hetero-nanostructured metal oxide-based hybrid photocatalysts for enhanced photoelectrochemical water splitting – a review, *Int. J. Hydrogen Energy*, 2020, **45**, 18331–18347.
- 43 J. Wu, X. Han, D. Li, B. E. Logan, J. Liu, Z. Zhang and Y. Feng, Efficient CO<sub>2</sub> conversion to formic acid in a novel microbial photoelectrochemical cell using a visible-light responsive Co<sub>3</sub>O<sub>4</sub> nanorod-arrayed photocathode, *Appl. Catal., B*, 2020, 276.
- 44 S. W. Eaton, M. Lai, N. A. Gibson, A. B. Wong, L. Dou, J. Ma, L. W. Wang, S. R. Leone and P. Yang, Lasing in robust cesium lead halide perovskite nanowires, *Proc. Natl. Acad. Sci. U. S. A.*, 2016, **113**, 1993–1998.
- 45 M. Li, Z. Zhao, T. Cheng, A. Fortunelli, C. Y. Chen, R. Yu, Q. Zhang, L. Gu, B. V. Merinov, Z. Lin, E. Zhu, T. Yu, Q. Jia, J. Guo, L. Zhang, W. A. Goddard 3rd, Y. Huang and X. Duan, Ultrafine jagged platinum nanowires enable ultrahigh mass activity for the oxygen reduction reaction, *Science*, 2016, **354**, 1414–1419.
- 46 T. Cai, Y. Huang, M. Huang, Y. Xi, D. Pang and W. Zhang, Enhancing oxygen reduction reaction of supercapacitor microbial fuel cells with electrospun carbon nanofibers composite cathode, *Chem. Eng. J.*, 2019, **371**, 544–553.
- 47 H. Wu, W. Zhang, S. Kandambeth, O. Shekhah, M. Eddaoudi and H. N. Alshareef, Conductive metal–organic frameworks selectively grown on laser-scribed graphene for electrochemical microsupercapacitors, *Adv. Energy Mater.*, 2019, **9**, 1900482.
- 48 L. Yang, G. Yi, Y. Hou, H. Cheng, X. Luo, S. G. Pavlostathis, S. Luo and A. Wang, Building electrode with three-dimensional macroporous interface from biocompatible polypyrrole and conductive graphene nanosheets to achieve highly efficient microbial electrocatalysis, *Biosens. Bioelectron.*, 2019, **141**, 111444.
- 49 Y. Liang, H. Feng, D. Shen, N. Li, Y. Long, Y. Zhou, Y. Gu, X. Ying and Q. Dai, A high-performance photo-microbial desalination cell, *Electrochim. Acta*, 2016, **202**, 197–202.
- 50 Q. Zhao, J. Yang, M. Liu, R. Wang, G. Zhang, H. Wang, H. Tang, C. Liu, Z. Mei, H. Chen and F. Pan, Tuning electronic push/pull of Ni-based hydroxides to enhance hydrogen and oxygen evolution reactions for water splitting, *ACS Catal.*, 2018, **8**, 5621–5629.
- 51 J. Schneider, M. Matsuoka, M. Takeuchi, J. Zhang, Y. Horiuchi, M. Anpo and D. W. Bahnemann, Understanding TiO<sub>2</sub> photocatalysis: mechanisms and materials, *Chem. Rev.*, 2014, **114**, 9919–9986.
- 52 D. Luan, L. Wu, T. Wei, L. Liu, Y. Lv, F. Yu, L. Chen and Y. Shi, N, S Dual-Doped carbon derived from dye sludge by using polymeric flocculant as soft template, *Nanomaterials*, 2019, **9**, 57.